Egyptian Journal of Chemistry

http://ejchem.journals.ekb.eg/

Microspectroscopic, DFT and QSAR Study of PVP/CaCO₃ Blends

as Potential Bone-Remineralization Membranes

Ahmed Refaat[a,b,*], Medhat Ibrahim[a]

[a]*Molecular Spectroscopy and Modeling Unit, Spectroscopy Department, National Research Centre, 33 El-Bohouth Str. 12622 Dokki, Giza, Egypt*

[b]*Synchrotron-Light for Experimental Science and Applications in the Middle East (SESAME), Allan, Jordan*

Abstract

Correlation between microscopy, spectroscopy, and molecular modeling is essential for elucidating the reactivity of biomaterials based on their electronic; physical and surface properties. Consequently, FTIR microspectroscopy (FTIRM) was used to study Poly(*N*-vinylpyrrolidone) (PVP) and PVP-CaCO₃ films prepared via the solution casting method. FTIR spectra confirmed the physical interaction between PVP and CaCO₃, thus indicating the availability of the functional groups of both compounds for further interaction. DFT molecular modeling calculations at B3LYP/6-31G (d, p) basis set were performed on PVP, CaCO₃, and four proposed schemes of interaction between both of them, and the structure's stability was examined in terms of total energy, while electronic properties were investigated in terms of total dipole moment, HOMO-LUMO band gap energy (ΔE), and molecular electrostatic potential maps (MESP). QSAR calculations were also performed to monitor the reactivity of the four proposed PVP-CaCO₃ interactions. The obtained FTIRM, molecular modeling, and QSAR results highlighted the suitability of the PVP-CaCO₃ blend for potential application as a biomaterial, such as bone-remineralization membrane.

Keywords: PVP-CaCO₃; FTIRM; B3LYP/6-31G (d, p); HOMO-LUMO; MESP; QSAR.

1. Introduction

Bone is a hard living tissue that makes up the skeleton, and is a hierarchically structured composite material of mineral and organic components [1,2]. The mineral or inorganic component of the bones is a calcium phosphate mineral known as hydroxyapatite, with the chemical formula $Ca_{10}(PO_4)_6(OH)_2$, while the organic component is collagen [3,4]. The formation of the bone matrix mainly takes place through first the deposition of the organic matrix, then followed by mineralization [5,6]. The bone formation process involves continuous remodeling of the bone tissue, including bone resorption by osteoclasts and bone formation by osteoblasts; however, the disruption between both processes leads to alteration of bone composition and can result in bone diseases including osteoporosis [5,7].

Bone quality is highly dependent on the quantity of mineralized tissue present, which in turn depends on different other factors including morphology, microarchitecture, collagen content and integrity, and mineralization [8]. Bone loss is the condition describing the loss of bone mass, resulting in the weakening of the bones and increased risk for fracture [9]. It results from trauma, as well as degenerative diseases such as osteoporosis which is associated with reduced density of the bone minerals [10]. Consequently, bone grafts (autografts and allografts) are considered the best treatment option for bone repair, except that autografts face serious challenges such as limited availability and donor-site morbidity [10]. On the other hand, biomaterial allografts are considered the second-best option after autografts, owing to their availability in large quantities, as well as availability in different types, forms, and properties

which include biocompatibility, bioactivity, and non-immunogenicity, thus being able to integrate well with the host tissue [10-12].

Poly(N-vinylpyrrolidone) (PVP) is an important water-soluble polymer produced via the polymerization of N-vinylpyrrolidone monomer [13]. The biocompatibility of PVP qualified it to be applied in various biomedical and pharmaceutical applications such as tissue-equivalent materials and a binder in many pharmaceutical tablets [14]. Several studies have reported different biomedical applications of PVP such as dressings and skin regeneration [15-20], bone repair and regeneration [21-30], improving hemo- and biocompatibility [31,32], dental implants [33,34], as well as many other different biomedical and pharmaceutical applications [35].

Fourier transform infrared (FTIR) spectroscopy is a versatile, powerful, and sensitive technique that is used to study the molecular composition of so many systems and structures, by determining the functional groups both qualitatively and quantitatively in the samples under analysis [36]. FTIR spectroscopy has been actively and continuously utilized in studying biomaterials [37]. It has been implemented in studying hydroxyapatite and its composites, and with different dopants [38-42], immunoregulatory cell-free biomaterials implanted into periodontal multi-tissue defects [43], immobilization of active substances on biomaterial substrates for medical applications [44], silk biomaterials applied in tissue engineering applications [45], novel hydrogels based on whey protein isolate for tissue regeneration [46], polymeric and bioactive glass-modified composite films loaded with polyphenols for bone tissue engineering. [47], and degradable biomaterials based on acetal moieties for bone regeneration [48].

Different methods and levels of theory of molecular modeling have been employed in computational studies of bone components, as well as materials intended for bone regeneration applications [49]. Density functional theory (DFT) was employed to calculate the adsorption of polycaprolactone on pure and doped hydroxyapatite [50]. DFT was also utilized to study the surface structures and properties of pure and silicate-substituted hydroxyapatite [51] and to study the interaction of collagen peptides with hydroxyapatite surfaces [52]. The inhibition of hydroxyapatite by phosphocitrate was theoretically studied using DFT calculations [53]. Molecular dynamics approaches have been implemented to study the adsorption of bone morphogenetic protein-2 (BMP-2) on surfaces of hydrophobic graphite and hydrophilic titanium dioxide rutile [54], and also its adsorption behavior with four initial orientations on hydrophobic gold and hydrophilic silicon nitride substrates [49]. PM5 semiempirical quantum mechanical calculations were conducted to study the interaction between chitosan and hydroxyapatite [55]. Molecular modeling was used to study chitosan/dopamine/ Fe_2O_3 as an effective nanocomposite for tissue engineering applications [56]. Four-body corrected fragment molecular orbital calculations at the MP2 level were employed to study hydroxyapatite–peptide interaction [57]. PM6 semiempirical, Hartree-Fock, and DFT calculations were carried out to calculate the thermal parameters of carbonated hydroxyapatite [58], and PM6 semiempirical level was used to study the interaction between carbonated hydroxyapatite and zinc oxide [59]. DFT and different experimental characterization techniques were used to study PVP films filled with cadmium sulfide (CdS) nanoparticles via in-situ preparation technique. Results demonstrated that CdS nanoparticles are stabilized by chemical interaction with PVP [60]. PVP matrices doped with silver and gold were also prepared by simple casting method and studied using DFT [61]. Simple casting method was also used to prepare Chitosan/PVP blend with different concentrations of ZnS nanoparticles, the properties of which were experimentally investigated, in addition to computational DFT approach [62].

In this study, the interaction between PVP and calcium carbonate ($CaCO_3$) is investigated using FTIR microspectroscopy for potential application as bone-remineralization membranes, since $CaCO_3$ is the primary structural mineral in the body. The electronic properties and quantitative structure-activity relationship (QSAR) of the proposed interaction schemes between PVP and $CaCO_3$ are also investigated using DFT molecular modeling calculations. To the best of our knowledge, this is the first study to report on the correlation between FTIR microspectroscopy, molecular modeling and QSAR in studying the reactivity of PVP polymeric matrix prepared via simple solution casting method and incorporated with $CaCO_3$ for possible application as bone remineralization membrane.

2. Experimental
2.1. Materials
Calcium carbonate was purchased from Daejung Reagents Chemicals, South Korea. Polyvinylpyrrolidone (PVP K-30) was purchased from Golden Bell Reactivos, Mexico.

2.2. Sample preparation
PVP and PVP-$CaCO_3$ films were prepared using the solution casting method. 1 gram of PVP was dissolved in 100 ml of distilled water via continuous stirring until complete dissolution of PVP and a clear solution

is obtained. PVP solution was then cast in plastic Petri dishes and left for 5 days to dry at room temperature.

1 M solution of $CaCO_3$ was prepared by dispersing 1 gram of $CaCO_3$ powder in 10 ml of distilled water, via continuous stirring for 2 hrs to ensure complete dispersion. PVP/$CaCO_3$ film was then prepared by adding 0.5 ml of $CaCO_3$ solution dropwise to 20 ml PVP solution with continuous stirring for 2 hrs. The obtained solution was finally cast in plastic Petri dishes and left for 5 days to dry at room temperature.

2.3. Fourier Transform Infrared (FTIR) microspectroscopy

FTIR microspectroscopy measurements of the prepared films were performed at the Infrared Beamline of Synchrotron-light for Experimental Science and Applications in the Middle East (SESAME) in Jordan. The spectra were acquired in transmission mode using the globar source of Thermo Nicolet 8700 FTIR spectrometer coupled with Thermo Nicolet Continuum IR microscope equipped with an MCT (Mercury Cadmium Telluride) detector. OMNIC v. 9.2.41 software package (Thermo Fisher Scientific, USA) was used for both data acquisition and data analysis. Spectra were recorded in the mid-infrared spectral range of 4000-650 cm^{-1} with a spectral resolution of 4 cm^{-1}, with 128 co-added scans for the samples and 256 co-added scans for the background, levels of zero filling: 0 with Happ-Genzel apodization window. The IR area maps of the samples were acquired with Atlμs v. 9.1.24 mapping software (Thermo Fisher Scientific, USA) using the 15X Schwarzschild objective and a matching 15x condenser.

2.4. Molecular Modeling Calculations

The model molecules for $CaCO_3$ and 3-unit (trimer) PVP were built using Gaussview 5.0 [63], and the geometry optimization and molecular modeling calculations were performed using Gaussian09 program [64] at Spectroscopy Department, National Research Centre (NRC), Egypt. Geometry optimization was done using Density Functional Theory (DFT) with the basis set of B3LYP/6-31G (d, p) [65-67]. A total of four interaction schemes between PVP and $CaCO_3$ were proposed, such that $CaCO_3$ was assumed to interact with PVP via weak bonding, once through the oxygen atom of the middle PVP unit, and once through the oxygen atom of one of the terminal units, and this interaction is assumed to take place once through the calcium atom of $CaCO_3$ and once through oxygen atom. Total dipole moment (TDM), HOMO-LUMO band gap energy (ΔE), molecular electrostatic potential (MESP) maps, and theoretical IR spectra

were also all calculated at the same level of theory to confirm that the calculated structures are corresponding to minimum energy, and to confirm the optimum structure and validating the obtained calculations.

2.5. Quantitative structure-activity relationship (QSAR)

QSAR modeling was performed using SCIGRESS 3.0 modeling and dynamics software suite [68] at Spectroscopy Department, National Research Centre, Egypt. A number of descriptors were estimated to fully assess the QSAR of the proposed interactions. The estimated descriptors were polar surface area (P-area), solvent-accessible polar surface area (Acc. P-area), ionization potential (IP), number of hydrogen-bond donor sites (HBD), and number of hydrogen-bond acceptor sites (HBA).

3. Results and discussion

3.1. FTIR Microspectroscopy

The FTIR spectra of pure PVP and PVP-$CaCO_3$ films in the range of 1800-800 cm^{-1} are shown in Fig. 1. The FTIR spectrum of pure PVP depicted its typical characteristic bands mentioned in the literature [69-75]. The band at 1664 cm^{-1} is attributed to C=O stretching vibration while the one at 1626 cm^{-1} could be attributed to OH bending of absorbed water. The bands in the range of 1495-1425 cm^{-1} are corresponding to C–H$_n$ deformations. CH$_2$ bending is represented by the band at 1375 cm^{-1}. The two bands at 1292 and 1020 cm^{-1} are attributed to C-N stretching. The bands at 1227, 1173, and 845 cm^{-1} are ascribed to C-C stretching, deformation vibration of the aromatic rings, and CH$_2$ bending, respectively.

In the FTIR spectrum of PVP-$CaCO_3$ film, all of the characteristic bands of PVP are still clearly seen which suggests that the interaction between PVP and $CaCO_3$ is a physical blend rather than a chemical complex [59,76]. The major difference in the spectrum of PVP-$CaCO_3$ when compared to that of pure PVP is the emergence of the characteristic bands of $CaCO_3$ at 1471-1444, 876, and 710 cm^{-1} representing bending vibrations of the carbonate group [59,77,78].

FTIR microspectroscopy also provides chemical maps depicting the chemical distribution of specific components, functional groups, or spectral regions in color-coded images, in which red areas represent high signal intensity, while blue areas represent low signal intensity [79,80].
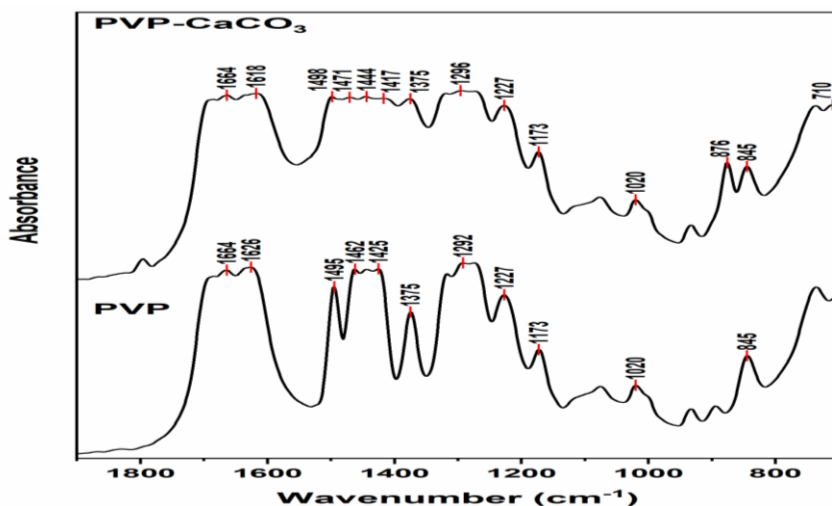
Figure 1: FTIR absorbance spectra of PVP and PVP-CaCO$_3$ membranes

Consequently, as shown in Fig. 2, two chemigram maps were generated for each sample over the 1500-1400 cm^{-1} and 920-820 cm^{-1} spectral regions which are common regions hosting characteristic bands of PVP and CaCO$_3$ as mentioned in the spectral analysis.

From the generated chemigram maps, it is easy to visually notice the difference in the chemical distribution pattern in the defined spectral regions between PVP and PVP-CaCO$_3$ blend films, owing to the presence of different functional groups corresponding to different chemical components related to PVP and CaCO$_3$.
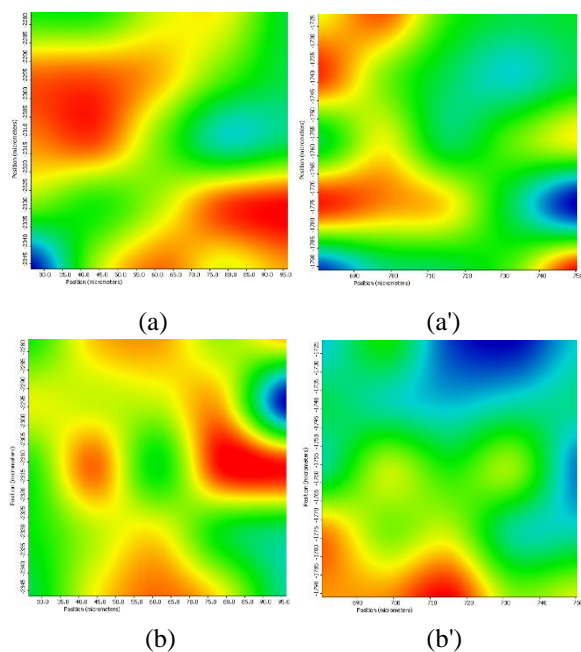

(a)   (a')

(b)   (b')

Figure 2: FTIRM chemigram maps of the 1500-1400 cm^{-1} region of (a) PVP and (a') PVP-CaCO$_3$, and of the 920-820 cm^{-1} region of (b) PVP and (b') PVP-CaCO$_3$. The chemigram scale bars are expressed in μm.

3.2. Molecular Modeling

3.2.1. Building model molecules

Based on the obtained FTIR microspectroscopy results which confirmed that the interaction between PVP and CaCO$_3$ is a physical one, thus allowing the functional groups of both compounds to be available for further interaction with the surrounding medium, and consequently has a direct effect on the overall reactivity of the PVP-CaCO$_3$ blend, it is important to further investigate the possible interactions and resulting structures to follow their effect on the reactivity. As a first step, it is important to demonstrate how the molecules were built. Fig. 3(a) shows the optimized structure of trimer (3-unit) PVP molecule and Fig. 3(b) shows the optimized structure of CaCO$_3$ molecule. The PVP trimer is composed of 18 carbon atoms, 29 hydrogen atoms, 3 oxygen atoms, and 3 nitrogen atoms. The oxygen atom in each PVP unit is linked to a carbon atom by a double bond, exactly at carbon atoms number C15, C19, and C23. From the demonstrated structures and in correlation with the obtained FTIR microspectroscopy results, physical interaction in the form of weak bond or electrostatic attraction such as hydrogen bond or Van der Waals attractions is assumed to take place between PVP and CaCO$_3$ through one of the oxygen atoms of the PVP trimer, once through the oxygen atom of the middle PVP unit (mid O), and once through the oxygen atom of one of the terminal units (term O). In addition, this interaction is assumed to take place once through the calcium atom of CaCO$_3$ (mid O-Ca and term O-Ca), and once through its oxygen atom bonded to the carbon atom (mid O-O and term O-O). Therefore, four proposed schemes of interaction will be investigated.

To understand the reactivity of the studied structures, molecular modeling is the best candidate for elucidating the reactivity of a given compound [81]. Furthermore, modeling data confirm those obtained

from spectroscopy [82,83]. The modeling parameters such as TDM, ΔE, as well as MESP are considered as excellent indicators for the reactivity of the studied structures, as reported earlier in the previous findings [84,85]. To validate the obtained modeling data, one can calculate the vibrational spectra at the same level of theory, to confirm that the structures are real structures in terms of positive frequencies [86].

It must be noted that DFT is a valuable and widely accepted computational method that has the advantage of describing electron correlation at a reasonable computational cost [87,88]. Additionally, a good balance can be achieved between placed and localized bond structures using the B3LYP method, hence B3LYP/6-31G (d, p) basis set was applied in many studies for the calculation of HOMO-LUMO band gap energies [88].

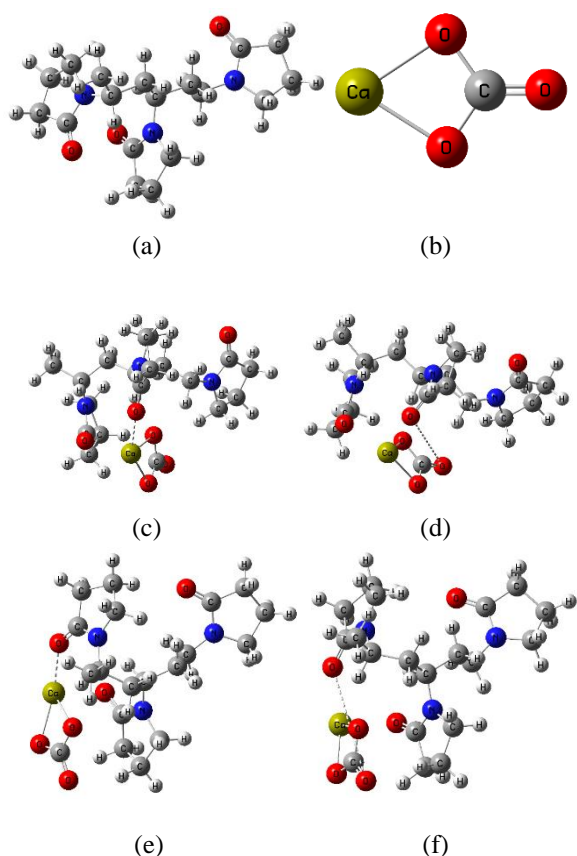The optimized structures of PVP, CaCO₃, and their four proposed interaction schemes are shown in Fig. 3.

(a)   (b)

(c)   (d)

(e)   (f)

Figure 3: Optimized structures of (a) PVP, (b) CaCO₃, (c) PVP-CaCO₃ (mid O-Ca), (d) PVP-CaCO₃ (mid O-O), (e) PVP-CaCO₃ (term O-Ca), and (f) PVP-CaCO₃ (term O-O)

The DFT computed IR spectra are demonstrated in Fig. 4. The theoretical IR spectra of PVP and PVP-CaCO₃ were computed and compared to the experimentally obtained FTIR spectra, and also to

confirm that the resulting optimized structures are real structures and confirming that the structures are corresponding to minimum energy.
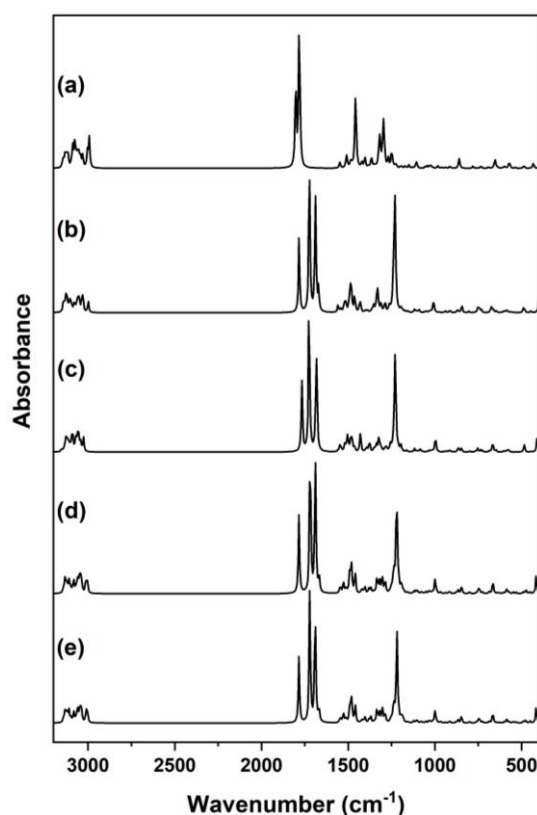

Figure 4: DFT computed IR spectra of (a) PVP, (b) PVP-CaCO3 Mid Ca, (c) PVP-CaCO3 Mid O, (d) PVP-CaCO3 Term Ca, (e) PVP-CaCO3 Term O-O

All of the DFT computed IR spectra of the optimized structures yielded positive frequencies, confirming that the structures are real [59]. The characteristic bands of PVP and PVP-CaCO₃ blends in the theoretically computed IR spectra are close to those obtained in the experimental spectrum. Similar to the experimental FTIR spectrum, the computed IR spectrum of pure PVP demonstrated a main band at ~1700 cm^{-1} corresponding to C=O stretching vibration, with multiple bands in the range of 1485-1420 cm^{-1} arising from C–H$_n$ deformations. The CH bending vibrations appeared at ~1320 cm^{-1}, while the band attributed to C-N stretching appeared at 1295 cm^{-1}. The difference between the spectral features of PVP (Fig. 4a), and PVP-CaCO₃ blends (Fig. 4b, c, d, and e) can also be easily and clearly observed.

_____

3.2.2. Total energy, total dipole moment, and HOMO-LUMO band gap energy

The energies of the highest occupied molecular orbital (HOMO) and lowest unoccupied molecular orbital (LUMO), and their difference (HOMO-LUMO band gap energy (ΔE)) [89], as well as the total energy of a given structure, are very important physical parameters in describing the stability of this structure, such that the lower the total energy the more stable the structure is [90,91], while the higher the ΔE the more stable the structure is [88,89,92]. On the other hand, TDM is used to detect the nature of reactivity of a given structure or system, and it is well established in several studies that TDM is closely related to reactivity in such a way that the higher the TDM, the higher the reactivity [93-95]. In addition to TDM, ΔE also plays an important role in describing the reactivity in such a way that high ΔE is indicative of lower reactivity while low ΔE is indicative of higher reactivity [89,82].

Table 1 lists the total energy, TDM, and ΔE of the optimized structures calculated at B3LYP/6-31G (d, p). As shown in the table, the total energy has significantly decreased upon the interaction of PVP with CaCO$_3$, reaching very close values among the four proposed schemes of interaction. This indicates that the four schemes of interaction resulted in much more stable structures than PVP and CaCO$_3$ individually.

In terms of reactivity, the values of TDM and ΔE were in perfect agreement with each other, and it is clear from the calculated values that all of the interaction schemes resulted in structures with higher reactivity than PVP. From the obtained values, the interaction scheme of PVP-CaCO$_3$ (term O-O) had the highest TDM of 14.8063 Debye and the lowest ΔE of 2.9393 eV, confirming that this is the most reactive structure among the proposed interaction schemes. The calculated HOMO-LUMO orbitals for PVP, CaCO3, and the four proposed interaction schemes are demonstrated in Fig. 5.

Table 1. Values of total energy, TDM, and HOMO-LUMO band gap energy calculated at B3LYP/6-31G (d, p) for PVP, CaCO$_3$, and their four proposed interaction schemes.

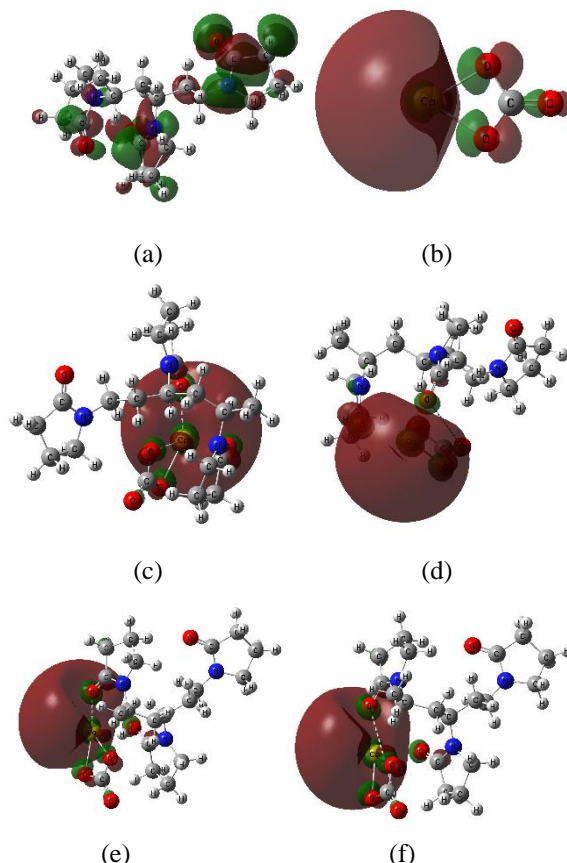| Structure	Total energy (KeV)	TDM (Debye)	ΔE (ev)
PVP	-29.7534	4.3608	7.1174
CaCO$_3$	-25.6157	14.6362	1.1733
PVP-CaCO$_3$ (mid O-Ca)	-55.3726	11.8992	3.0909
PVP-CaCO$_3$ (mid O-O)	-55.3726	10.5961	3.0879
PVP-CaCO$_3$ (term O-Ca)	-55.3724	14.6691	2.9491
PVP-CaCO$_3$ (term O-O)	-55.3724	14.8063	2.9393

_____

Fig. 5. DFT HOMO-LUMO frontier molecular orbitals calculated at B3LYP/6-31G (d, p) for (a) PVP, (b) CaCO$_3$, (c) PVP-CaCO$_3$ (mid O-Ca), (d) PVP-CaCO$_3$ (mid O-O), (e) PVP-CaCO$_3$ (term O-Ca), and (f) PVP-CaCO$_3$ (term O-O)

3.2.3. Molecular electrostatic potential

MESP is simply a color-coded map of the electrostatic potential based on the constant electron density surface that is created by the nuclei and electrons of a molecule in the surrounding space [96,97]. It is a commonly known and well-established method to study and predict the molecular behavior of interaction, by determining the sites of high electron density (red color) available for attack by electrophiles, and the sites of low electron density (blue color) available for attack by nucleophiles [96-98]. The MESP maps obtained in this study are displayed in Fig. 6.

As seen in the figure, it is obvious that the sites of high electron density are the oxygen atom of the C=O group of PVP units, as well as those of the CaCO$_3$ molecule, indicating that those sites are susceptible to attack by electrophiles. The blue color surrounding the calcium atom of the CaCO$_3$ molecule clearly reflects the low

electron density at this site, making it available for attack by nucleophiles.

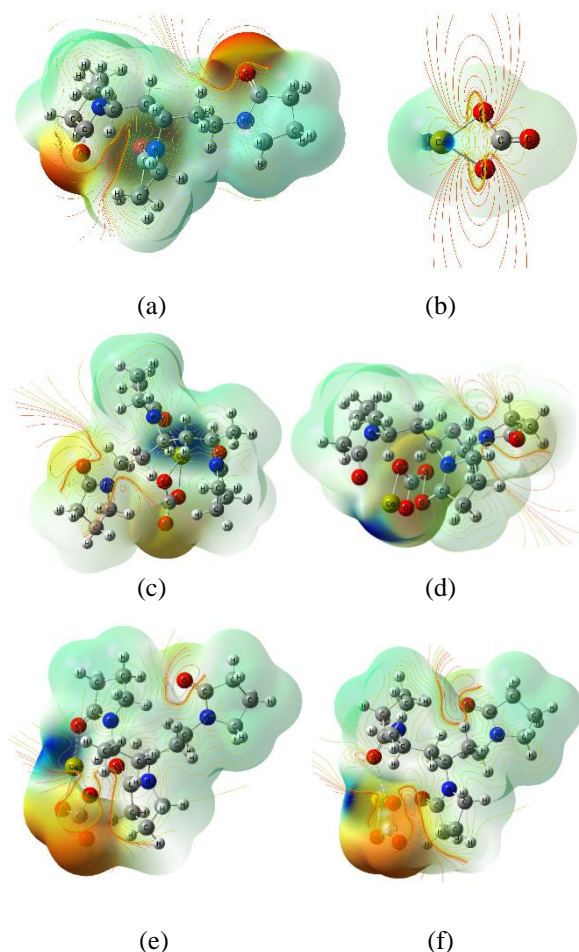
(a)   (b)

(c)   (d)

(e)   (f)

Fig. 6. MESP maps calculated at B3LYP/6-31G (d, p) for (a) PVP, (b) CaCO₃, (c) PVP-CaCO₃ (mid O-Ca), (d) PVP-CaCO₃ (mid O-O), (e) PVP-CaCO₃ (term O-Ca), and (f) PVP-CaCO₃ (term O-O)

3.3. Quantitative structure-activity relationship

QSAR is a computational modeling method that has been applied in numerous scientific studies to study the relationship between the chemical structure of compounds and their biological activities [99]. This relationship is described through a number of numerical values called descriptors, resulting from the QSAR computational model [100]. In the current study, the descriptors used to investigate the QSAR of PVP and PVP-CaCO₃ blends are P-area, Acc. P-area, IP, HBD, and HBA.

The P-area is defined as the sum of the molecular surface of polar atoms, including nitrogen and oxygen atoms and any hydrogen atoms attached to them [101], and describes the physical interaction of the surface of the molecule that is to take place through its electrostatic potential [102]. Acc. P-area is the surface area of both electronegative and electropositive atoms

that is accessible to a polar solvent, such as water, for interaction [102], such that the larger the solvent Acc. P-area, the higher solubility and lower lipophilicity which would be desirable to molecules intended to be present in a water medium [103]. IP is the amount of energy required to ionize a structure, thus reflecting also its reactivity [91]. Finally, HBD and HBA are simply the number of sites of hydrogen-bond donors and hydrogen-bond acceptors, respectively, showing the capability of the molecule to form hydrogen bonds [103].

Table 2 lists the calculated values of the QSAR descriptors for PVP, CaCO₃, and the four schemes of interaction of the PVP-CaCO₃ blend. As shown in the table, the P-area and Acc. P-area of the four schemes of interaction of the PVP-CaCO₃ blend are noticeably larger than those of PVP, which indicates higher solubility and lower lipophilicity, with PVP-CaCO₃ (term O-O) having the highest value of both descriptors. The IP of the four schemes of interaction of the PVP-CaCO₃ blend came lower than that of PVP and CaCO₃ indicating higher reactivity of the blend, with again PVP-CaCO₃ (term O-O) showing the lowest IP value, suggesting that it is more reactive than the rest of the interaction schemes. Finally, all the studied structures had zero HBD, but demonstrated varying numbers of HBA sites, revealing the capability of all the structures to participate in the formation of hydrogen bonds.

Table 2. QSAR descriptors calculated at B3LYP/6-31G (d, p) for PVP, CaCO₃, PVP-CaCO₃ (mid O-Ca), PVP-CaCO₃ (mid O-O), PVP-CaCO₃ (term O-Ca), and PVP-CaCO₃ (term O-O)

Structure	P-area ($Å^2$)	Acc. P-area ($Å^2$)	IP (kJ/mol)	HBD	HBA
PVP	62.41	36.4	37.44	0	6
CaCO₃	78.62	70.63	31.06	0	3
PVP-CaCO₃ (mid O-Ca)	193.52	116.4	28.6	0	8
PVP-CaCO₃ (mid O-O)	165.77	97.16	27.98	0	9
PVP-CaCO₃ (term O-Ca)	199.72	125.64	27.16	0	9
PVP-CaCO₃ (term O-O)	201.85	126.2	27.12	0	9

_____

The number of HBA sites in the four schemes of interaction of the PVP-CaCO$_3$ blend was higher than that of PVP, indicating the relatively higher number of hydrogen bonds they can participate in forming.

4. Conclusion

FTIRM results indicated that PVP and CaCO$_3$ interacted physically as the functional groups of both compounds are still present. The interaction was further studied using DFT calculations at B3LYP/6-31G (d, p) level in terms of total energy, TDM, ΔE, and MESP. Based on both TDM and ΔE results, it is clear that all of the PVP-CaCO$_3$ interaction schemes resulted in structures with higher reactivity than PVP. The interaction scheme of PVP-CaCO$_3$ (term O-O) had the highest TDM and lowest ΔE, confirming that this is the most reactive structure among the proposed interaction schemes. MESP maps confirmed that the sites of high electron density are the oxygen atom of the C=O group of PVP, as well as those of the CaCO$_3$ molecule, indicating that those sites are susceptible to attack by electrophiles. While the calcium atom of the CaCO$_3$ molecule clearly reflects the low electron density at this site, making it available for attack by nucleophiles.

QSAR descriptors indicated that, the P-area and Acc. P-area of the four schemes of interaction of the PVP-CaCO$_3$ blend are noticeably larger than those of PVP, which indicates higher solubility and lower lipophilicity, with PVP-CaCO$_3$ (term O-O) having the highest value of both descriptors. The IP of the four schemes of interaction of the PVP-CaCO$_3$ blend came lower than that of PVP and CaCO$_3$ indicating higher reactivity of the blend. The PVP-CaCO$_3$ (term O-O) showed the lowest IP value, indicating that it is more reactive than other schemes. Finally, all schemes showed zero HBD sites, with varying values of HBA sites, indicating that all studied structures are able to participate in the formation of hydrogen bonds. Correlating the above results, one can conclude that the obtained FTIRM, molecular modeling, and QSAR results highlighted the suitability of the PVP-CaCO$_3$ blend for potential application as a biomaterial, such as a bone-remineralization membrane. As a general conclusion, microscopy, spectroscopy, and molecular modeling could be correlated to indicate the reactivity of casted PVP and PVP-CaCO$_3$ films.

5. Conflicts of interests

There are no conflicts to declare.

6. Funding

7. References

[1] S.V. Euw, Y. Wang, G. Laurent, C. Drouet, F. Babonneau, N. Nassif, T. Azaïs, Bone mineral: new insights into its chemical composition, Sci. Rep. 9 (2019) 8456. https://doi.org/10.1038/s41598-019-44620-6

[2] S.R. Stock, The Mineral–Collagen Interface in Bone, Calcif. Tissue Int. 97 (3) (2015) 262–280. https://doi.org/10.1007/s00223-015-9984-6

[3] G. Ulian, D. Moro, G. Valdrè, Hydroxylapatite and Related Minerals in Bone and Dental Tissues: Structural, Spectroscopic and Mechanical Properties from a Computational Perspective, Biomolecules 11 (2021) 728. https://doi.org/10.3390/biom11050728

[4] G. Pezzotti, A. Rondinella, E. Marin, W. Zhu, N.N. Aldini, G. Ulian, G. Valdrè, Raman spectroscopic investigation on the molecular structure of apatite and collagen in osteoporotic cortical bone, J. Mech. Behav. Biomed. 65 (2017) 264-273. https://doi.org/10.1016/j.jmbbm.2016.08.030

[5] R. Florencio-Silva, G.R. Sasso, E. Sasso-Cerri, M.J. Simões, P.S. Cerri, Biology of Bone Tissue: Structure, Function, and Factors That Influence Bone Cells, Biomed. Res. Int. 2015 (2015) 421746. https://doi.org/10.1155%2F2015%2F421746

[6] H. Ping, H. Xie, Y. Wan, Z. Zhang, J. Zhang, M. Xiang, J. Xie, H. Wang, W. Wang, Z. Fu, Confinement controlled mineralization of calcium carbonate within collagen fibrils, J. Mater. Chem. B 4 (2016) 880-886. https://doi.org/10.1039/C5TB01990G

[7] J. Katz, I. Rotstein, Prevalence of Periapical Lesions in Patients with Osteoporosis, J. Endodont. 47 (2) (2021) 234-238. https://doi.org/10.1016/j.joen.2020.10.019

[8] A.L. Boskey, Bone composition: relationship to bone fragility and antiosteoporotic drug effects, Bonekey Rep. 2 (2013) 447. https://doi.org/10.1038%2Fbonekey.2013.181

[9] D.E. Whittier, L.A. Burt, S.K. Boyd, A new approach for quantifying localized bone loss by measuring void spaces, Bone 143 (2021) 115785. https://doi.org/10.1016/j.bone.2020.115785

_____

[10] A.A. Thorpe, C. Freeman, P. Farthing, J. Callaghan, P.V. Hatton, I.M. Brook, C. Sammon, C.L. Le Maitre, *In vivo* safety and efficacy testing of a thermally triggered injectable hydrogel scaffold for bone regeneration and augmentation in a rat model, Oncotarget 9 (26) (2018) 18277-18295. https://doi.org/10.18632/oncotarget.24813

[11] W. Wang, K.W.K. Yeung, Bone grafts and biomaterials substitutes for bone defect repair: A review, Bioactive Materials 2 (2017) 224-247. http://dx.doi.org/10.1016/j.bioactmat.2017.05.007

[12] R. Agarwal, A.J. García, Biomaterial strategies for engineering implants for enhanced osseointegration and bone repair, Adv. Drug Deliver. Rev. 94 (1) (2015) 53-62. https://doi.org/10.1016/j.addr.2015.03.013

[13] X. Liu, Y. Xu, Z. Wu, H. Chen, Poly(*N*-vinylpyrrolidone)-Modified Surfaces for Biomedical Applications, Macromol. Biosci. 13 (2013) 147–154. https://doi.org/10.1002/mabi.201200269

[14] M.Y. Kariduraganavar, A.A. Kittur, R.R. Kamble, Polymer Synthesis and Processing, in: S.G. Kumbar, C.T. Laurencin, M. Deng (Eds.), Natural and Synthetic Biomedical Polymers, Elsevier, Amsterdam, 2014, pp. 1-31. https://doi.org/10.1016/B978-0-12-396983-5.00001-6

[15] E. Biazar, Z. Roveimiab, G. Shahhosseini, M. Khataminezhad, M. Zafari, A. Majdi, Biocompatibility Evaluation of a New Hydrogel Dressing Based on Polyvinylpyrrolidone/Polyethylene Glycol, J. Biomed. Biotechnol. 2012 (2012) 343989. https://doi.org/10.1155/2012/343989

[16] M.H. Casimiro, S.R. Gomes, G. Rodrigues, J.P. Leal, L.M. Ferreira, Chitosan/poly (vinylpyrrolidone) matrices obtained by gamma-irradiation for skin scaffolds: Characterization and preliminary cell response studies, Materials (Basel) 11 (12) (2018) 2535. https://doi.org/10.3390/ma11122535

[17] N. Aghamohamadi, N.S. Sanjani, R.F. Majidi, S.A. Nasrollahi, Preparation and characterization of Aloe vera acetate and electrospinning fibers as promising antibacterial properties materials, Mater. Sci. Eng. C. 94 (2019) 445–452. https://doi.org/10.1016/j.msec.2018.09.058

[18] A.R. Sadeghi-avalshahr, S. Nokhasteh, A.M. Molavi, N. Mohammad-pour, M. Sadeghi, Tailored PCL Scaffolds as Skin Substitutes Using Sacrificial PVP Fibers and Collagen/Chitosan Blends, Int. J. Mol. Sci. 21 (2020) 2311. https://doi.org/10.3390/ijms21072311

[19] K. Li, D. Wang, K. Zhao, K. Song, J. Liang, Electrohydrodynamic jet 3D printing of PCL/PVP composite scaffold for cell culture, Talanta 211 (2020) 120750. https://doi.org/10.1016/j.talanta.2020.120750

[20] S.G. Sheish, R. Emadi, M. Ahmadian, S. Sadeghzade, F. Tavangarian, Fabrication and Characterization of Polyvinylpyrrolidone-Eggshell Membrane-Reduced Graphene Oxide Nanofibers for Tissue Engineering Applications, Polymers 13 (2021) 913. https://doi.org/10.3390/polym13060913

[21] Y. Zhang, T. Wang, J. Li, X. Cui, M. Jiang, M. Zhang, X. Wang, W. Zhang, Z. Liu, Bilayer Membrane Composed of Mineralized Collagen and Chitosan Cast Film Coated with Berberine-Loaded PCL/PVP Electrospun Nanofiber Promotes Bone Regeneration, Front. Bioeng. Biotechnol. 9 (2021) 684335. https://doi.org/10.3389/fbioe.2021.684335

[22] M. Dau, C. Ganz, F. Zaage, B. Frerich, T. Gerber, Hydrogel-embedded nanocrystalline hydroxyapatite granules (elastic blocks) based on a cross-linked polyvinylpyrrolidone as bone grafting substitute in a rat tibia model, Int. J. Nanomed. 12 (2017) 7393–7404. http://dx.doi.org/10.2147/IJN.S142550

[23] S.U. Maheshwari, K. Govindan, M. Raja, A. Raja, M.B.S. Pravin, S.V. Kumar, Preliminary studies of PVA/PVP blends incorporated with HAp and β-TCP bone ceramic as template for hard tissue engineering, Bio-Med. Mater. Eng. 28 (2017) 401–415. https://doi.org/10.3233/BME-171682

[24] N. Saha, R. Shah, P. Gupta, B.B. Mandal, R. Alexandrova, M.D. Sikiric, P. Saha, PVP - CMC hydrogel: An excellent bioinspired and biocompatible scaffold for osseointegration, Mater. Sci. Eng. C. 95 (2019) 440–449. https://doi.org/10.1016/j.msec.2018.04.050

[25] X. Cao, X. Cai, R. Chen, H. Zhang, T. Jiang, Y. Wang, A thermosensitive chitosan-based hydrogel for sealing and lubricating purposes in dental implant system, Clin. Implant Dent. Relat. Res. 21 (2019) 324–335. https://doi.org/10.1111/cid.12738

[26] M. Ghosh, S.C. Jana, Fabrication of Hollow and Porous Tin-Doped Indium Oxide Nanofibers and Microtubes via a Gas Jet Fiber Spinning Process, Materials (Basel) 13 (2020) 1539. https://doi.org/10.3390/ma13071539

[27] D. Anandan, S. Mary Stella, N. Arunai Nambiraj, U. Vijayalakshmi, A.K. Jaiswal, Development of mechanically compliant 3D composite scaffolds for bone tissue engineering applications, J. Biomed. Mater. Res. - Part A.

106 (2018) 3267–3274. https://doi.org/10.1002/jbm.a.36525

[28] P. Basu, N. Saha, R. Alexandrova, B. Andonova-Lilova, M. Georgieva, G. Miloshev, P. Saha, Biocompatibility and biological efficiency of inorganic calcium filled bacterial cellulose based hydrogel scaffolds for bone bioengineering, Int. J. Mol. Sci. 19 (12) (2018) 3980. https://doi.org/10.3390/ijms19123980

[29] P. Basu, N. Saha, R. Alexandrova, P. Saha, Calcium phosphate incorporated bacterial cellulose-polyvinylpyrrolidone based hydrogel scaffold: Structural property and cell viability study for bone regeneration application, Polymers (Basel) 11 (11) (2019) 1821. https://doi.org/10.3390/polym11111821

[30] J. Hou, Y. Wang, H. Xue, Y. Dou, Biomimetic growth of hydroxyapatite on electrospun CA/PVP core-shell nanofiber membranes, Polymers (Basel) 10 (9) (2018) 1032. https://doi.org/10.3390/polym10091032

[31] I. Łojszczyk, A. Kuźmińska, B.A. Butruk-Raszeja, T. Ciach, Fenton-type reaction grafting of polyvinylpyrrolidone onto polypropylene membrane for improving hemo- and biocompatibility, Mat. Sci. Eng. C-Mater. 113 (2020) 110960. https://doi.org/10.1016/j.msec.2020.110960

[32] M. Sun, H. Qiu, C. Su, X. Shi, Z. Wang, Y. Ye, Y. Zhu, Solvent-Free Graft-from Polymerization of Polyvinyl Pyrrolidone Imparting Ultra-Low Bacterial Fouling and Improved Biocompatibility, ACS Appl. Bio. Mater. 2 (9) (2019) 3983-3991. https://doi.org/10.1021/acsabm.9b00529

[33] S. Tort, A. Yıldız, F. Tuğcu-Demiröz, G. Akca, Ö. Kuzukıran, F. Acartürk, Development and characterization of rapid dissolving ornidazole loaded PVP electrospun fibers, Pharm. Dev. Technol. 24 (2019) 864–873. https://doi.org/10.1080/10837450.2019.1615088

[34] P. He, Q. Zhong, Y. Ge, Z. Guo, J. Tian, Y. Zhou, S. Ding, H. Li, C. Zhou, Dual drug loaded coaxial electrospun PLGA/PVP fiber for guided tissue regeneration under control of infection, Mater. Sci. Eng. C. 90 (2018) 549–556, https://doi.org/10.1016/j.msec.2018.04.014

[35] M. Kurakulaa, K. Rao G.S.N., Moving polyvinyl pyrrolidone electrospun nanofibers and bioprinted scaffolds toward multidisciplinary biomedical applications, Eur. Polym. J. 136 (2020) 109919. https://doi.org/10.1016/j.eurpolymj.2020.109919

[36] A.A. Kamnev, Y.A. Dyatlova, O.A. Kenzhegulov, A.A. Vladimirova, P.V. Mamchenkova, A.V. Tugarova, Fourier Transform Infrared (FTIR) Spectroscopic Analyses of Microbiological Samples and Biogenic Selenium Nanoparticles of Microbial Origin: Sample Preparation Effects, Molecules 26 (4) (2021) 1146. https://doi.org/10.3390%2Fmolecules26041146

[37] J.A. Kimber, S.G. Kazarian, Spectroscopic imaging of biomaterials and biological systems with FTIR microscopy or with quantum cascade lasers, Anal. Bioanal. Chem. 409 (2017) 5813–5820. https://doi.org/10.1007/s00216-017-0574-5

[38] M. Wojcik, P. Kazimierczak, A. Belcarz, A. Wilczynska, V. Vivcharenko, L. Pajchel, L. Adaszek, A. Przekora, Biocompatible curdlan-based biomaterials loaded with gentamicin and Zn-doped nano-hydroxyapatite as promising dressing materials for the treatment of infected wounds and prevention of surgical site infections, Biomaterials Advances 139 (2022) 213006. https://doi.org/10.1016/j.bioadv.2022.213006

[39] I. Uysal, F. Severcan, Z. Evis, Characterization by Fourier transform infrared spectroscopy of hydroxyapatite co-doped with zinc and fluoride, Ceram. Int. 39 (2013) 7727–7733. http://dx.doi.org/10.1016/j.ceramint.2013.03.029

[40] R.-X. Sun, Y. Lv, Y.-R. Niu, X.-H. Zhao, D.-S. Cao, J. Tang, X.-C. Sun, K.-Z. Chen, Physicochemical and biological properties of bovine-derived porous hydroxyapatite/collagen composite and its hydroxyapatite powders, Ceram. Int. 43 (18) (2017) 16792-16798. https://doi.org/10.1016/j.ceramint.2017.09.075

[41] K.C.V. Kumar, T.J. Subha, K.G. Ahila, B. Ravindran, S.W. Chang, A.H. Mahmoud, O.B. Mohammed, M.A. Rathi, Spectral characterization of hydroxyapatite extracted from Black Sumatra and Fighting cock bone samples: A comparative analysis, Saudi J. Biol. Sci. 28 (2021) 840–846. https://doi.org/10.1016/j.sjbs.2020.11.020

[42] A. Pal, S. Paul, A.R. Choudhury, V.K. Balla, M. Das, A. Sinha, Synthesis of hydroxyapatite from *Lates calcarifer* fish bone for biomedical applications, Mater. Lett. 203 (2017) 89-92. http://dx.doi.org/10.1016/j.matlet.2017.05.103

[43] G. Liu, X. Zhou, L. Zhang, Y. Zou, J. Xue, R. Xia, N. Abuduxiku, X. Gan, R. Liu, Z. Chen, Y. Cao, Z. Chen, Cell-free immunomodulatory biomaterials mediated *in situ* periodontal multi-tissue regeneration and their

immunopathophysiological processes, Materials Today Bio 16 (2022) 100432. https://doi.org/10.1016/j.mtbio.2022.100432

[44] D. Kowalczuk, M. Pitucha, Application of FTIR Method for the Assessment of Immobilization of Active Substances in the Matrix of Biomedical Materials, Materials 12 (2019) 2972. https://doi.org/10.3390/ma12182972

[45] K. Lau, C. Heu, M.J. Moore, A. Zhang, B. Akhavan, S.G. Wise, M.M.M. Bilek, M.S. Lord, J. Rnjak-Kovacina, Effect of plasma ion immersion implantation on physiochemical and biological properties of silk towards creating a versatile biomaterial platform, Materials Today Advances 13 (2022) 100212. https://doi.org/10.1016/j.mtadv.2022.100212

[46] M. Dziadek, K. Charuza, R. Kudlackova, J. Aveyard, R. D'Sa, A. Serafim, I.-C. Stancu, H. Iovu, J.G. Kerns, S. Allinson, K. Dziadek, P. Szatkowski, K. Cholewa-Kowalska, L. Bacakova, E. Pamula, T.E.L. Douglas, Modification of heat-induced whey protein isolate hydrogel with highly bioactive glass particles results in promising biomaterial for bone tissue engineering, Mater. Design 205 (2021) 109749. https://doi.org/10.1016/j.matdes.2021.109749

[47] M. Dziadek, K. Dziadek, K. Checinska, B. Zagrajczuk, M. Golda-Cepa, M. Brzychczy-Wloch, E. Menaszek, A. Kopec, K. Cholewa-Kowalska, PCL and PCL/bioactive glass biomaterials as carriers for biologically active polyphenolic compounds: Comprehensive physicochemical and biological evaluation, Bioactive Materials 6 (2021) 1811–1826. https://doi.org/10.1016/j.bioactmat.2020.11.025

[48] B. Dellago, A. Ricke, T. Geyer, R. Liska, S. Baudis, Photopolymerizable precursors for degradable biomaterials based on acetal moieties, Eur. Polym. J. 154 (2021) 110536. https://doi.org/10.1016/j.eurpolymj.2021.110536

[49] I. Marquetti, S. Desai, Molecular modeling the adsorption behavior of bone morphogenetic protein-2 on hydrophobic and hydrophilic substrates, Chem. Phys. Lett. 706 (2018) 285–294. https://doi.org/10.1016/j.cplett.2018.06.015

[50] J. Song, X. Li, N. Cui, X. Lu, J. Yun, Q. Huang, Y. Sun, E.-S. Lee, H. Jiang, Zn and Ag Doping on Hydroxyapatite: Influence on the Adhesion Strength of High-Molecular Polymer Polycaprolactone, Molecules 27 (2022) 1928. https://doi.org/10.3390/molecules27061928

[51] Z. Liu, L. Zhang, X. Wang, G. Jiang, M. Yang, A comparative study of the dissolubility of pure and silicon substituted hydroxyapatite from

[52] N. Almora-Barrios, N.H. de Leeuw, A Density Functional Theory Study of the Interaction of Collagen Peptides with Hydroxyapatite Surfaces, Langmuir 26 (18) (2010) 14535–14542. https://doi.org/10.1021/la101151e

[53] A. Wierzbickia, H.S. Cheung, Molecular modeling of inhibition of hydroxyapatite by phosphocitrate, J. Mol. Struc-Theochem. 529 (2000) 73–82. https://doi.org/10.1016/S0166-1280(00)00534-0

[54] T. Utesch, G. Daminelli, M.A. Mroginski, Molecular Dynamics Simulations of the Adsorption of Bone Morphogenetic Protein-2 on Surfaces with Medical Relevance, Langmuir 27 (2011) 13144–13153. https://dx.doi.org/10.1021/la202489w

[55] E.M. El-Sayed, A. Omar, M. Ibrahim, W.I. Abdel-Fattah, On the Structural analysis and Electronic Properties of Chitosan/Hydroxyapatite Interaction, J. Comput. Theor. Nanosci. 6 (2009) 1663-1669. https://doi.org/10.1166/jctn.2009.1228

[56] N. El-Sayed, M. El-Bakary, M. Ibrahim, M. ELgamal, Molecular Modeling Analysis of Chitosan-Dopamine Blend with Iron Oxide Nanoparticles for Tissue Engineering Applications, Biointerface Research in Applied Chemistry 11 (5) (2021) 12483-12494. https://doi.org/10.33263/BRIAC115.1248312494

[57] K. Kato, K. Fukuzawa, Y. Mochizuki, Modeling of hydroxyapatite–peptide interaction based on fragment molecular orbital method, Chem. Phys. Lett. 629 (2015) 58–64. https://doi.org/10.1016/j.cplett.2015.03.057

[58] R.A. Youness, M.A. Taha, H. Elhaes, M. Ibrahim, Molecular modeling, FTIR spectral characterization and mechanical properties of carbonated-hydroxyapatite prepared by mechanochemical synthesis, Mater. Chem. Phys. 190 (2017) 209-218. https://doi.org/10.1016/j.matchemphys.2017.01.004

[59] A. Refaat, R.A. Youness, M.A. Taha, M. Ibrahim, Effect of zinc oxide on the electronic properties of carbonated hydroxyapatite, J. Mol. Struct. 1147 (2017) 148-154. https://doi.org/10.1016/j.molstruc.2017.06.091

[60] A.M. Abdelghany, E.M. Abdelrazek, D.S. Rashad, Impact of in situ preparation of CdS filled PVP nano-composite. Spectrochim Acta A 130 (2014) 302-308. https://doi.org/10.1016/j.saa.2014.04.049

[61] A. M. Abdelghany, M.S. Mekhail, E.M. Abdelrazek, M.M. Aboud, Combined

_____

DFT/FTIR structural studies of monodispersed PVP/Gold and silver nano particles. J. Alloy Compd. 646 (2015) 326-332. https://doi.org/10.1016/j.jallcom.2015.05.262

[62] A.M. Abdelghany, M.S. Meikhail, A.H. Oraby, M.A. Aboelwafa, Experimental and DFT studies on the structural and optical properties of chitosan/polyvinyl pyrrolidone/ZnS nanocomposites. Polym. Bull. (2023) 1-20. https://doi.org/10.1007/s00289-023-04700-0

[63] A.B. Nielsen, A.J. Holder, GaussView 5.0, User's Reference, GAUSSIAN Inc., Pittsburgh (2009).

[64] Gaussian 09, Revision C.01, Frisch M., Trucks G., Schlegel H., Scuseria G., Robb M., Cheeseman J., Scalmani G., Barone V., Mennucci B., Petersson G., Nakatsuji H., Caricato M., Li X., Hratchian H., Izmaylov A., Bloino J., Zheng G., Sonnenberg J., Hada M., Ehara M., Toyota K., Fukuda R., Hasegawa J., Ishida M., Nakajim T., Honda Y., Kitao O., Nakai H., Vreven Y., Montgomery J., Peralta J.Jr., Ogliaro F., Bearpark M., Heyd J., Brothers E., Kudin K., Staroverov V., Keith T., Kobayashi R., Normand J., Raghavachari K., Rendell A., Burant J., Iyengar S., Tomasi J., Cossi M., Rega N., Millam J., Klene M., Knox J., Cross J., Bakken V., Adamo C., Jaramillo J., Gomperts R., Stratmann R., Yazyev O., Austin A., Cammi R., Pomelli C., Ochterski J., Martin R., Morokuma K., Zakrzewski V., Voth G., Salvador P., Dannenberg J., Dapprich S., Daniels A., Farkas O., Foresman J., Ortiz J., Cioslowski J., Fox D., Gaussian, Inc., Wallingford CT, 2010.

[65] A.D. Becke, Density-functional thermochemistry. III. The role of exact exchange, Chem. Phys. 98 (1993) 5648-5652. https://doi.org/10.1063/1.464913

[66] C. Lee, W. Yang, R.G. Parr, Development of the Colle-Salvetti correlation-energy formula into a functional of the electron density, Phys. Rev. B 37 (2) (1998) 785. https://doi.org/10.1103/PhysRevB.37.785

[67] B. Miehlich, A. Savin, H. Stoll, H. Preuss, Results obtained with the correlation energy density functionals of becke and Lee, Yang and Parr, Chem. Phys. Lett. 157 (3) (1989) 200-206. https://doi.org/10.1016/0009-2614(89)87234-3

[68] Stewart J.J.P. Fujitsu Limited; Sunnyvale, Calif, USA: 2009. SCIGRESS. Version 2.9.0.

[69] I. Sriyanti, L. Marlina, A. Fudholi, S. Marsela, J. Jauhari, Physicochemical properties and *In vitro* evaluation studies of polyvinylpyrrolidone/cellulose acetate composite nanofibres loaded with *Chromolaena odorata* (L) King extract, J.

Mater. Res. Technol. 12 (2021) 333-342. https://doi.org/10.1016/j.jmrt.2021.02.083

[70] H. Fakhry, M. El-Sonbati, B. Omar, R. El-Henawy, Y. Zhang, M. EL-Kady, Novel fabricated low-cost hybrid polyacrylonitrile/polyvinylpyrrolidone coated polyurethane foam (PAN/PVP@PUF) membrane for the decolorization of cationic and anionic dyes, J. Environ. Manage. 315 (2022) 115128. https://doi.org/10.1016/j.jenvman.2022.115128

[71] H.M. Zidan, E.M. Abdelrazek, A.M. Abdelghany, A.E. Tarabiah, Characterization and some physical studies of PVA/PVP filled with MWCNTs, J. Mater. Res. Technol. 8 (1) (2019) 904–913. https://doi.org/10.1016/j.jmrt.2018.04.023

[72] B. Singh, A. Kumar, Development of dietary fibre moringa gum and polyvinylpyrrolidone based hydrogels for drug delivery application, Food Hydrocolloids for Health 1 (2021) 100008. https://doi.org/10.1016/j.fhfh.2021.100008

[73] L.K. Mireles, M.-R. Wu, N. Saadeh, L. Yahia, E. Sacher, Physicochemical Characterization of Polyvinyl Pyrrolidone: A Tale of Two Polyvinyl Pyrrolidones, ACS Omega 5 (47) (2020) 30461–30467. https://doi.org/10.1021%2Facsomega.0c04010

[74] E. Erizal, T. Tjahyono, P.P. Dian, D. Darmawan, Synthesis of polyvinyl pyrrolidone (PVP)/K-carrageenan hydrogel prepared by gamma radiation processing as a function of dose and PVP concentration, Indones. J. Chem. 13 (2013) 41–46.

[75] B. Paruzel, J. Pfleger, J. Brus, M. Menšík, F. Piana, U. Acharya, Impact of Hydrogen Bonds Limited Dipolar Disorder in High-k Polymer Gate Dielectric on Charge Carrier Transport in OFET, Polymers 12 (4) (2020) 826. https://doi.org/10.3390/polym12040826

[76] Y. Wu, L.-D. Liao, H.-C. Pan, L. He, C.-T. Lin, M.C. Tan, Fabrication and interfacial characteristics of surface modified Ag nanoparticle based conductive composites, RSC Adv. 7 (2017) 29702–29712. https://doi.org/10.1039/c7ra04657j

[77] M. Fathy, M.A. Zayed, Y.M. Moustafa, Synthesis and applications of CaCO$_3$/HPC core–shell composite subject to heavy metals adsorption processes, Heliyon 5 (2019) e02215. https://doi.org/10.1016/j.heliyon.2019.e02215

[78] S.F.A. Ali, M. El Batouti, M. Abdelhamed, E. El-Rafey, Formulation and characterization of new ternary stable composites: Polyvinyl chloride-wood flourcalcium carbonate of promising physicochemical properties, J. Mater. Res.

_____

Technol. 9 (6) (2020) 12840–12854. https://doi.org/10.1016/j.jmrt.2020.08.113

[79] M.M. Mata-Miranda, A. Martinez-Cuazitl, C.I. Guerrero-Robles, J.E. Noriega-Gonzalez, J.S. Garcia-Hernandez, G.J. Vazquez-Zapien, Biochemical similarity between cultured chondrocytes and *in situ* chondrocytes by chemometric analysis from FTIR microspectroscopy, Biotechnology Reports 24 (2019) e00391. https://doi.org/10.1016/j.btre.2019.e00391

[80] A.M. Abdelghany, H.A. ElBatal, Optical and µ-FTIR mapping: a new approach for structural evaluation of V₂O₅-lithium fluoroborate glasses. Mater. Design 89 (2016) 568-572. https://doi.org/10.1016/j.matdes.2015.09.159

[81] M. Ibrahim, O. Osman, Spectroscopic Analyses of Cellulose: Fourier Transform Infrared and Molecular Modelling Study, J. Comput. Theor. Nanosci. 6 (5) (2009) 1054–1058. https://doi.org/10.1166/jctn.2009.1143

[82] A.M.F. Galal, E.M. Shalaby, A. Abouelsayed, M.A. Ibrahim, E. Al-Ashkar, A.G Hanna, Structure and absolute configuration of some 5-Chloro-2-methoxy-N-phenylbenzamide derivatives, Spectrochim. Acta A. 188 (2018) 213-221. https://doi.org/10.1016/j.saa.2017.06.068

[83] A.M.F. Galal, D. Atta, A. Abouelsayed, M.A. Ibrahim, A.G. Hanna, Configuration and Molecular Structure of 5-Chloro-N-(4-sulfamoylbenzyl) Salicylamide Derivatives, Spectrochim. Acta A. 214 (2019) 476–486. https://doi.org/10.1016/j.saa.2019.02.070

[84] A.M. Bayoumy, M. Ibrahim, A. Omar, Mapping Molecular Electrostatic Potential (MESP) for Fulleropyrrolidine and its Derivatives, Opt. Quant. Electron. 52 (2020) 346. https://doi.org/10.1007/s11082-020-02467-6

[85] P. Grenni, A.B. Caracciolo, L. Mariani, M. Cardoni, C. Riccucci, H. Elhaes, M.A. Ibrahim, Effectiveness of a new green technology for metal removal from contaminated water, Microchem. J. 147 (2019) 1010-1020. https://doi.org/10.1016/j.microc.2019.04.026

[86] M. Ibrahim, E. Koglin, Spectroscopic study of Polyaniline Emeraldine Base: Modelling Approach, Acta Chim. Slov. 52 (2005) 159-163.

[87] C.C. Peterson, D.A. Penchoff, J.D. Auxier II, H.L. Hall, Establishing Cost-Effective Computational Models for the Prediction of Lanthanoid Binding in [Ln(NO₃)]²⁺ (with Ln = La to Lu), ACS Omega 4 (1) (2019) 1375–1385. https://doi.org/10.1021/acsomega.8b02403

[88] Ü. Yildiko, A.C. Ata, İ. Cakmak, Synthesis, spectral characterization and DFT calculations of novel macro MADIX agent: mechanism of addition-fragmentation reaction of xanthate compound, SN Applied Sciences 2 (2020) 1691. https://doi.org/10.1007/s42452-020-03495-3

[89] E.A. Eno, H. Louis, T.O. Unimuke, T.E. Gber, I.J. Mbonu, C.J. Ndubisi, S.A. Adalikwu, Reactivity, stability, and thermodynamics of para-methylpyridinium-based ionic liquids: Insight from DFT, NCI, and QTAIM, Journal of Ionic Liquids 2 (2022) 100030. https://doi.org/10.1016/j.jil.2022.100030

[90] A.M. Bayoumy, A. Refaat, I.S. Yahia, H.Y. Zahran, H. Elhaes, M.A. Ibrahim, M. Shkir, Functionalization of graphene quantum dots (GQDs) with chitosan biopolymer for biophysical applications, Opt. Quant. Electron. 52 (2020) 16. https://doi.org/10.1007/s11082-019-2134-z

[91] A.H. Al-Bagawi, A.M. Bayoumy, M.A. Ibrahim, Molecular modeling analyses for graphene functionalized with Fe₃O₄ and NiO, Heliyon 6 (2020) e04456. https://doi.org/10.1016/j.heliyon.2020.e04456

[92] M. Miar, A. Shiroudi, K. Pourshamsian, A.R. Oliaey, F. Hatamjafari, Theoretical investigations on the HOMO–LUMO gap and global reactivity descriptor studies, natural bond orbital, and nucleus-independent chemical shifts analyses of 3-phenylbenzo[d]thiazole-2(3H)-imine and its para-substituted derivatives: Solvent and substituent effects, J. Chem. Res. 45 (1-2) (2021) 147-158. https://doi.org/10.1177/1747519820932091

[93] J.D. Rush, J. Lan, W.H. Koppenol, Effect of a Dipole Moment on the Ionic Strength Dependence of Electron-Transfer Reactions of Cytochrome *c*, J. Am. Chem. Soc. 109 (9) (1987) 2679–2682. https://doi.org/10.1021/ja00243a020

[94] K. Durka, R. Kamiński, S. Luliński, J. Serwatowski, K. Woźniak, On the nature of the B···N interaction and the conformational flexibility of arylboronic azaesters, Phys. Chem. Chem. Phys. 12 (2010) 13126–13136. https://doi.org/10.1039/C0CP00030B

[95] M. Rezaei-Sameti, N.J. Jukar, A computational study of nitramide adsorption on the electrical properties of pristine and C-replaced boron nitride nanosheet, J. Nanostruct. Chem. 7 (2017) 293–307. https://doi.org/10.1007/s40097-017-0237-2

[96] E. Ourhzif, E. Ketatni, M. Akssira, Y. Troin, M. Khouili, Crystal structure, Hirshfeld surface analysis and DFT studies of *Euphorbioside* monohydrate a major bisnorsesquiterpene isolated from *Euphorbia resinifera* latex, J.

_____

Mol. Struct. 1241 (2021) 130511. https://doi.org/10.1016/j.molstruc.2021.130511

[97] W. Donglai, S. Hongtao, Z. Yuchun, Theoretical Study on Molecular Electrostatic Potential of C_{78}, J. Rare Earth 25 (2) (2007) 210-214. https://doi.org/10.1016/S1002-0721(07)60075-1

[98] G.P.S. Mol, D. Aruldhas, I.H. Joe, Chemical reactivity, molecular electrostatic potential and in-silico analysis on benzimidazole fungicide benomyl, Heliyon 8 (2022) e11417. https://doi.org/10.1016/j.heliyon.2022.e11417

[99] H. Hazhazi, N. Melkemi, T. Salah, M. Bouachrine, DFT-based reactivity and combined QSAR, molecular docking of 1,2,4,5-Tetrazine derivatives as inhibitors of Pim-1 kinase, Heliyon 5 (2019) e02451. https://doi.org/10.1016/j.heliyon.2019.e02451

[100] R. Pingaew, V. Prachayasittikul, A. Worachartcheewan, A. Thongnum, S. Prachayasittikul, S. Ruchirawat, V. Prachayasittikul, Anticancer activity and QSAR study of sulfur-containing thiourea and sulfonamide derivatives, Heliyon 8 (2022) e10067. https://doi.org/10.1016/j.heliyon.2022.e10067

[101] H.O. Tekin, G. ALMisned, S.A.M. Issa, E.S. Kasikci, M. Arooj, A. Ene, M.S. Al-Buriahi, M. Konuk, H.M.H. Zakaly, Molecular Polar Surface Area, Total Solvent Accessible Surface Area (SASA), Heat of Formation, and Gamma-Ray Attenuation Properties of Some Flavonoids, Front. Phys. 10 (2022) 838725. https://doi.org/10.3389/fphy.2022.838725

[102] G. Schaftenaar, J. de Vlieg, Quantum mechanical polar surface area, J. Comput. Aided Mol. Des. 26 (2012) 311–318. https://doi.org/10.1007/s10822-012-9557-y

[103] T.J. Ritchie, S.J.F. Macdonald, S.D. Pickett, Insights into the impact of N- and O-methylation on aqueous solubility and lipophilicity using matched molecular pair analysis, Med. Chem. Commun. 6 (2015) 1787-1797. https://doi.org/10.1039/C5MD00309A

_____